Ultramicroscopy 276 (2025) 114169

Contents lists available at ScienceDirect

Ultramicroscopy

journal homepage: www.elsevier.com/locate/ultramic

Momentum microscopy with combined hemispherical and time-of-flight electron analyzers at the soft X-ray beamline I09 of the diamond light source

Matthias Schmitt [a,b,1], Deepnarayan Biswas [a], Olena Tkach [c], Olena Fedchenko [c], Jieyi Liu [a], Hans-Joachim Elmers [c], Michael Sing [b], Ralph Claessen [b], Tien-Lin Lee [a], Gerd Schönhense [c,*]

[a] Diamond Light Source Ltd., Harwell Science and Innovation Campus, Didcot OX11 0DE, United Kingdom
[b] Physikalisches Institut and Würzburg-Dresden Cluster of Excellence ct.qmat, Julius-Maximilians-Universität, D-97074 Würzburg, Germany
[c] Institut für Physik, Johannes Gutenberg-Universität, D-55128 Mainz, Germany

ARTICLE INFO

Keywords:
Momentum microscopy
PEEM
XPEEM
Hemispherical analyzer
Time-of-flight analyzer

ABSTRACT

The three-dimensional recording scheme of time-of-flight momentum microscopes (ToF-MMs) is advantageous for fast mapping of the photoelectron distribution in (E,$\boldsymbol{k}$) parameter space over the entire Brillouin zone. However, the 2 ns pulse period of most synchrotrons is too short for pure ToF photoelectron spectroscopy. The use of a hemispherical analyzer (HSA) as a pre-filter allows ToF-MM at such high pulse rates. The first HSA & ToF hybrid MM is operated at the soft X-ray branch of beamline I09 at the Diamond Light Source, UK. The photon energy ranges from 105 eV to 2 keV, with circular polarization available for $h\nu \geq 145$ eV. The HSA reduces the transmitted energy band to typically 0.5 eV, which is then further analyzed by ToF recording. In initial experiments, the overall efficiency gain when switching from the standard 2D (k_x,k_y) mode to the 3D (k_x,k_y,E_{kin}) hybrid mode was about 24. This value is determined by the number of resolved kinetic energies (here 12) and the transmission gain of the electron optics due to the high pass energy of the HSA in hybrid mode (E_{pass} up to 500 eV). The transmission gain depends on the size of the photon footprint on the sample. Under k-imaging conditions, the energy and momentum resolution are 10.2 meV (FWHM) (4.2 meV with 200 μm slits and $E_{pass} = 8$ eV) and 0.010 Å^{-1}. The energy filtered X-PEEM mode showed a spatial resolution of 250 nm. As examples, we show 2D band mapping of bilayer graphene, 3D mapping of the Fermi surface of Cu, circular dichroic ARPES for intercalated indenene layers, and the *sp* valence band of Au. Full-field photoelectron diffraction patterns of Ge show rich structure in k-field diameters of up to 6 Å^{-1}.

1. Introduction

Photoelectron momentum microscopy, also called k-PEEM, has proven to be a powerful method for angle-resolved photoelectron spectroscopy (ARPES) [1,2] and refs. therein]. Such instruments record k_x–k_y images with diameters typically exceeding a full Brillouin zone. Double and single hemispherical or time-of-flight (ToF) analyzers are used as energy filters. The high collection efficiency of the objective lens of a momentum microscope (MM), typically a cathode lens with a high-voltage extractor electrode, allows observation over large angular ranges up to the full 2π solid angle. MMs can cover kinetic energies from near-threshold (laser-ARPES) up to the X-ray range.

After the pioneering work with a double-hemisphere laboratory instrument by Kirschner and Tusche [3,4], several hemisphere-based MMs have been installed at synchrotron radiation sources [1,5–7]. Experiments with ToF-MMs have been performed in the 40-bunch filling mode of PETRA III (DESY, Hamburg) using soft X-rays [8] and hard X-rays [9], even with photoelectron spin analysis [10]. In particular, soft X-ray momentum microscopy is well suited to map the photoelectron distribution in four-dimensional (E, $\boldsymbol{k}$) parameter space. The fixed sample geometry is advantageous for circular dichroism (CD-ARPES) or photoelectron diffraction (PED) experiments because it eliminates any modulation of the matrix element otherwise caused by changing the angle of incidence.

* Corresponding author.
E-mail address: schoenhe@uni-mainz.de (G. Schönhense).
[1] Present address: Carl Zeiss SMT GmbH, D-73447 Oberkochen, Germany.

https://doi.org/10.1016/j.ultramic.2025.114169
Received 20 December 2024; Received in revised form 4 May 2025; Accepted 16 May 2025
Available online 20 May 2025
0304-3991/© 2025 The Authors. Published by Elsevier B.V. This is an open access article under the CC BY license (http://creativecommons.org/licenses/by/4.0/).

Like the majority of synchrotron radiation sources worldwide, the Diamond Light Source (DLS) in Didcot, UK, operates almost exclusively at a pulse rate of about 500 MHz. This operating mode is not suitable for ToF-MM due to the short time interval of only 2 ns between the adjacent pulses. For such sources, the ToF technique can be implemented in two different ways: either the pulse rate is reduced via electron-optical pulse picking using a fast GHz-bandwidth deflector in the electron path, or the energy bandwidth is reduced by a dispersive bandpass filter, before the electrons enter the ToF analyzer [11]. The latter approach was followed in the present work.

We present a new end station at the soft X-ray branch of beamline I09 at the Diamond Light Source, UK. The key component is a large single hemispherical analyzer (HSA) with a path radius of 225 mm combined with a time-of-flight analyzer behind the exit slit. This 'hemisphere & ToF' hybrid momentum microscope allows two modes of operation: In the *HSA-only mode* we use the 2D (k_x,k_y) imaging scheme of hemisphere-based MMs. A low pass energy (20 – 40 eV) results in a resolution of typically 30 – 50 meV, matching the photon bandpass. 3D (k_x,k_y,E_{kin}) data sets are recorded sequentially by stepwise scanning of the sample bias. In *hemisphere & ToF hybrid mode,* the additional 'ToF booster' behind the exit slit of the HSA is used for energy discrimination [12]. The pass energy of the HSA is increased to 300 – 500 eV, resulting in a transmitted energy band of 0.5 – 0.9 eV.

The photon energy range of beamline I09 covers $h\nu = 105$ eV to 2 keV, allowing to vary the probing depth from highly surface sensitive to bulk sensitive. Variable polarization, including circular, is available for $h\nu \geq 145$ eV, allowing CD-ARPES measurements. A focused and monochromated He lamp is used for off-line measurements. Using He I excitation, a base resolution of 4.2 meV (FWHM) has been achieved with small analyzer slits (200 μm) and a pass energy of 8 eV [11]. Under conditions suitable for synchrotron experiments (E_{pass}= 10 eV and 400 μm slits), the instrument achieves an energy resolution of 10.2 meV.

The hemisphere & ToF hybrid mode of operation is novel for synchrotron-based experiments. The transit time spread due to different path lengths of the electrons in the analyzer is generally considered detrimental for time-resolved experiments with HSAs [13,14]. However, with *k*-resolved detection, the spread can be easily corrected numerically [11]. Momentum-resolved recording also circumvents the resolution limitation due to the α^2-aberration term [15], where α is the entrance angle into the analyzer.

After describing the setup and discussing the performance of the different modes, we show examples for several application cases: X-PEEM measurements on a test sample, band mapping of bilayer graphene, 3D energy surface mapping of bulk copper [Cu(111)], CD-ARPES for intercalated indenene layers and for the *sp* valence bands of Cu and Au, and a series of full-field photoelectron diffraction patterns of Ge.

2. Setup and characterization of the instrument

2.1. The setup at the I09 Beamline

The setup for **S**ynchrotron radiation based **A**dvanced **M**omentum **M**icroscop**y** (**SAMMy)** is installed at the soft X-ray branch of beamline I09 [16] at the Diamond Light Source. The instrument is embedded in a UHV endstation [Fig. 1(a)] consisting of a loadlock, distribution and storage chamber as well as a preparation chamber equipped with a water-cooled 4-axis manipulator with both a resistive and an electron-beam heater, an argon sputter gun, a LEED and further ports for user equipment like, e.g., evaporators. In addition, there is a dedicated port for mounting a UHV suitcase to the endstation enabling *in situ* sample transfer from other preparation facilities. The momentum microscope features a hexapod manipulator allowing a 6-axis sample alignment and liquid helium cooling for studies at cryogenic temperatures down to < 28 K. The base pressure of the microscope chamber is 1 × 10^{-10} mbar and reaches 6 × 10^{-11} mbar with liquid helium cooling.

Fig. 1(b) shows a scheme of the electron optical system. The central element is a large hemispherical analyzer with a path radius of R_0 = 225 mm (SPECS Phoibos 225 'special'). This analyzer transmits a specific energy band – depending on the pass energy and slit widths – while preserving the two-dimensional momentum distribution of the photoelectrons. The entrance lens column comprises the front lens and two zoom lens groups. The latter focus a magnified image of the sample first

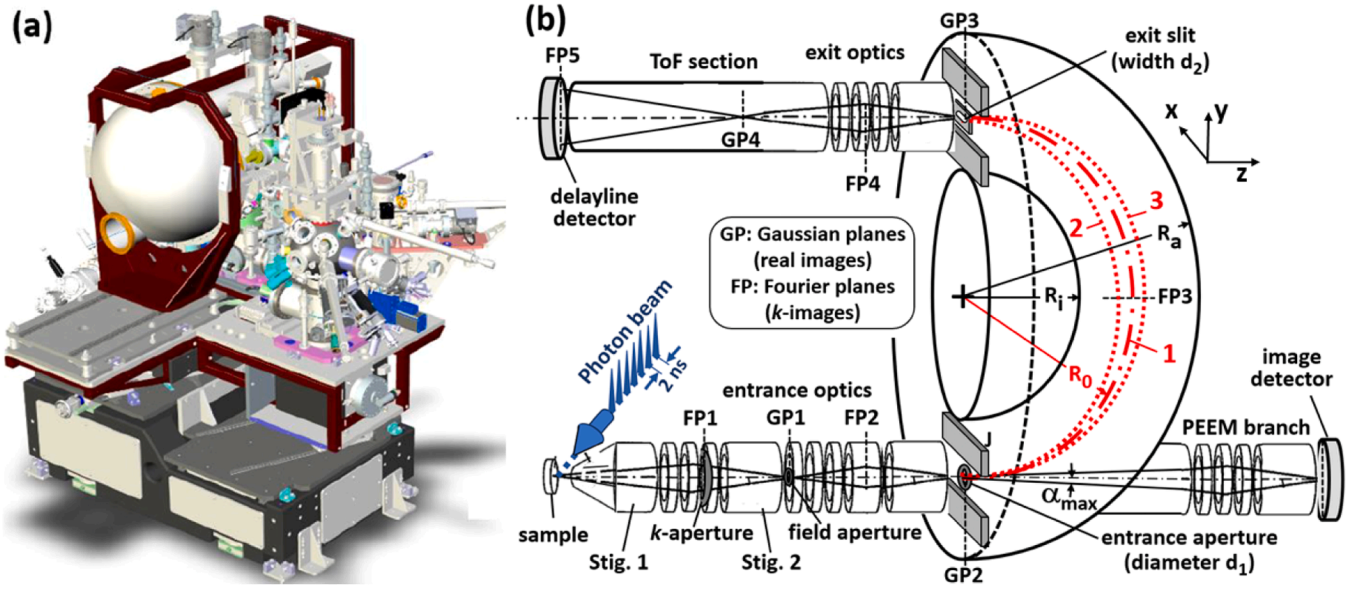

Fig. 1. The 'hemisphere & ToF' hybrid momentum microscope at the soft X-ray branch of I09 at the Diamond Light Source. (a) View of the complete setup with hemispherical analyzer and preparation equipment, all carried by an adjustable bench with 4 degrees of freedom (x,y,z,θ). θ is the angle of photon incidence, adjustable in a range of 0 – 20° with respect to the sample surface. (b) Cross sectional view of the electron-optical system, consisting of entrance lens, hemisphere for bandpass pre-filtering, exit lens and time-of-flight drift section followed by a delay-line detector (DLD). Two stigmators/deflectors (Stig. 1 and 2) are used for beam shaping and alignment. Arrays of *k*-apertures and field apertures allow optimization of the image contrast and selection of the size of the region of interest on the sample. FP1-5 and GP1-4 denote Fourier and Gaussian planes, respectively. PEEM imaging is possible using the straight branch with all hemisphere voltages set to the same value.

onto the intermediate image in Gaussian Plane 1 (GP1) and then into the entrance aperture (GP2). Two octupole stigmators/deflectors (Stig. 1 and 2) near Gaussian and reciprocal image planes allow beam alignment. Arrays with different sizes of *k*-apertures and field apertures are placed in Fourier Plane 1 (FP1) and real image plane 1 (GP1), respectively. They allow contrast optimization and selection of a region of interest on the sample. The hemispherical field acts as an imaging element and focuses the Gaussian image from GP1 (in the entrance aperture with diameter d_1) to the real image plane GP3 (in the exit slit with width d_2) while filtering the energy bandwidth. Finally, the exit lens system behind the analyzer converts the Gaussian image from the exit slit back into a momentum image on the delay-line detector (DLD) in the Fourier plane FP5 at the end of the ToF drift section. In X-PEEM mode the Gaussian image plane GP4 is focused on the DLD plane.

In hybrid mode, the high-speed delay-line detector disperses the incoming electron bunches -pre-filtered by the HSA- into thin time sections, determining the final energy resolution. An advantage of this hybrid-type MM scheme is its compatibility with continuous sources, in the present instrument a He lamp. At low pass energies the instrument works without ToF recording. Then only a single energy slice is measured at a time and energy series are measured sequentially. In this case (the *HSA-only mode*) the energy resolution is determined by the pass energy and analyzer slit widths. In *hybrid mode*, the analyzer pass energy is much higher and the final energy resolution is reached by ToF analysis. With all voltages of the HSA set to the same value, conventional PEEM imaging without energy filtering is possible in the straight-through PEEM branch. In this case, the combination of an MCP and a fluorescent screen serves as an image detector, which is captured by a CCD camera through a window.

Synchrotron radiation (standard fill pattern: 900 bunch train and 36 bunch gap) enters the microscope chamber through a flat bellow enabling angular rotation of the endstation under UHV. In combination with the heavy-duty rotary stage carrying the multi-chamber system, Fig. 1(a), this bellow allows for changing the angle of incidence from 0° (grazing incidence) up to 20° without the need to move the sample relatively to the extractor lens.

2.2. Characterization of the Instrument

The entrance lens of the hemispherical analyzer contains two piezo motor driven arrays of field apertures and contrast apertures that allow us to limit the accepted area on the sample and the acceptance angle, respectively. For the following measurement, to determine the instrumental energy resolution, we used focused He I radiation (21.2 eV) from a monochromated UV source (SPECS Sirius), analyzer entrance and exit apertures with diameters of $d_1 = d_2 = 400$ μm, and a pass energy of $E_{pass} = 10$ eV. Given the mean path radius of the hemisphere of $R_0 = 225$ mm (ray 1 in Fig. 1(b)), the theoretical energy resolution can be calculated as:

$$\Delta E_{HSA} = E_{pass} \cdot \frac{d_1 + d_2}{4 \cdot R_0} = 8.9 \text{ meV(FWHM)} \quad (1)$$

Since the hemisphere is used in k-imaging mode, the α^2-term does not affect the energy resolution as it can be easily corrected numerically in a 3D data stack. For the experimental determination, a Au(111) single crystal was freshly prepared by argon ion sputtering followed by thermal annealing to 500°C in the preparation chamber. The quality of the crystal surface was verified by observing the herring bone reconstruction in the LEED pattern. The sample was then placed in the liquid He cooled hexapod of the MM and the Fermi cutoff was measured. This measurement was performed in the HSA-only mode. By stepwise sweeping the sample bias, the small energy window defined by the pass energy and slit width is shifted across the spectrum. Unlike in conventional ARPES experiments, the sample bias here is set to a positive value ($U_{sa} = E_{kin}/e$), which is advantageous because the analyzer and the ToF section are kept at low voltages.

Patterns were recorded by scanning the sample bias in 2 mV steps and then integrating the intensity in the central region of the pattern, yielding the angle-integrated spectrum shown in Fig. 2(a). After deconvolution with thermal broadening at 28 K, the instrumental energy resolution was determined to be 10.2 meV and is thus in good agreement with the theoretical expectation. The base resolution of 4.2 meV of this instrument [11] has been achieved with 200 μm slits and $E_{pass} = 8$ eV.

To evaluate the momentum resolution, Fermi surface mapping of the gold crystal with high statistics was performed, which shows the well-known Shockley surface state around the Γ-point, Fig. 2(b). By varying the voltages of the exit lens column, we zoomed into the region near the Γ-point with an estimated lateral magnification factor of about 6. The Rashba splitting of 0.025 Å^{-1} is clearly resolved. Band maps along different directions in *k*-space can be extracted from the measured (k_x,k_y, E_{kin}) stack. Fig. 2(c) shows the dispersion of the surface state along the dashed line in (b). The Rashba splitting and the band crossing at the Γ-point around $E_B = 500$ meV are well resolved.

To quantify the *k*-resolution, a line profile was extracted along the dashed line as shown in (d), revealing four distinct peaks. The line profiles were fitted with a Voigt function (shown in blue). This function includes both the intrinsic lifetime broadening (approximated by a Lorentzian component) and the instrumental broadening (represented by a Gaussian component). Literature values [4] for the Lorentzian widths of the inner (0.0084 Å^{-1}) and outer (0.0065 Å^{-1}) ring were used. In this way, the momentum resolution was determined to be 0.010 Å^{-1}, which is a typical value for MMs.

An important parameter for practical work is the zoom range of the *k*-field of view, i.e., the possibility to access momentum images in maximum detail. This is of interest not only in the center of the image, as in Fig. 2(b), but also off-center, like around the K-points of many materials. Fig. 2(e) shows the Au Fermi surface map measured with synchrotron radiation at $h\nu = 120$ eV. The *k*-stigmator/deflector allows not only precise alignment of the momentum image to the detector, but also controlled displacement. This, in combination with the exit lens system, allows off-center zooming. Fig. 2(f) shows a zoomed section of the adjacent BZ marked with a blue circle.

Larger *k*-ranges are shown in Figs. 2(g-i), recorded at photon energies of 560 and 390 eV, respectively. A Cu(111) sample was chosen for the pattern in Fig. 2(g) to emphasize the instrument's sensitivity by resolving the faint narrow band features indicated by the arrows. Their origin will be discussed below in the context of Ref. [17]. Such narrow features do not appear for Au(111). Figures 2(a-g) were recorded in *HSA-only mode* with a pass energy of 30 eV. Fig. 2(h) was recorded in the *hemisphere & ToF hybrid mode* with a pass energy of the HSA of 500 eV. In this case, an energy band of 800 meV is simultaneously recorded as shown in (i). We clearly see the Shockley state S appearing in the second BZ, arrows in Fig. 2(h), which is surprising for such a high photon energy (390 eV).

2.3. Spectroscopic Real-space Imaging (XPEEM)

PEEM images without energy filtering can be recorded in 'straight-through mode' using an MCP screen assembly and a CCD camera mounted on a viewport behind the entrance aperture of the HSA (Fig. 1 (b), bottom right). In this mode, all hemisphere voltages are set to the same value so that the beam is not deflected and the image is focused only by the entrance optics. This mode is useful for quickly inspecting the sample surface, searching for small sample flakes, and selecting a homogeneous area on the surface. Fig. 3(a) shows a PEEM image of a calibration sample taken in the straight branch. This object consists of horizontal and vertical stripe arrays of Au on Si with a periodicity of 5 μm. The sample was illuminated by the He lamp (21.2 eV) and the microscope optics were set to maximum intensity, close to the low-energy cutoff. The contrast in such PEEM images is composed of work function and topographic contrast. The bright region corresponds to the photon

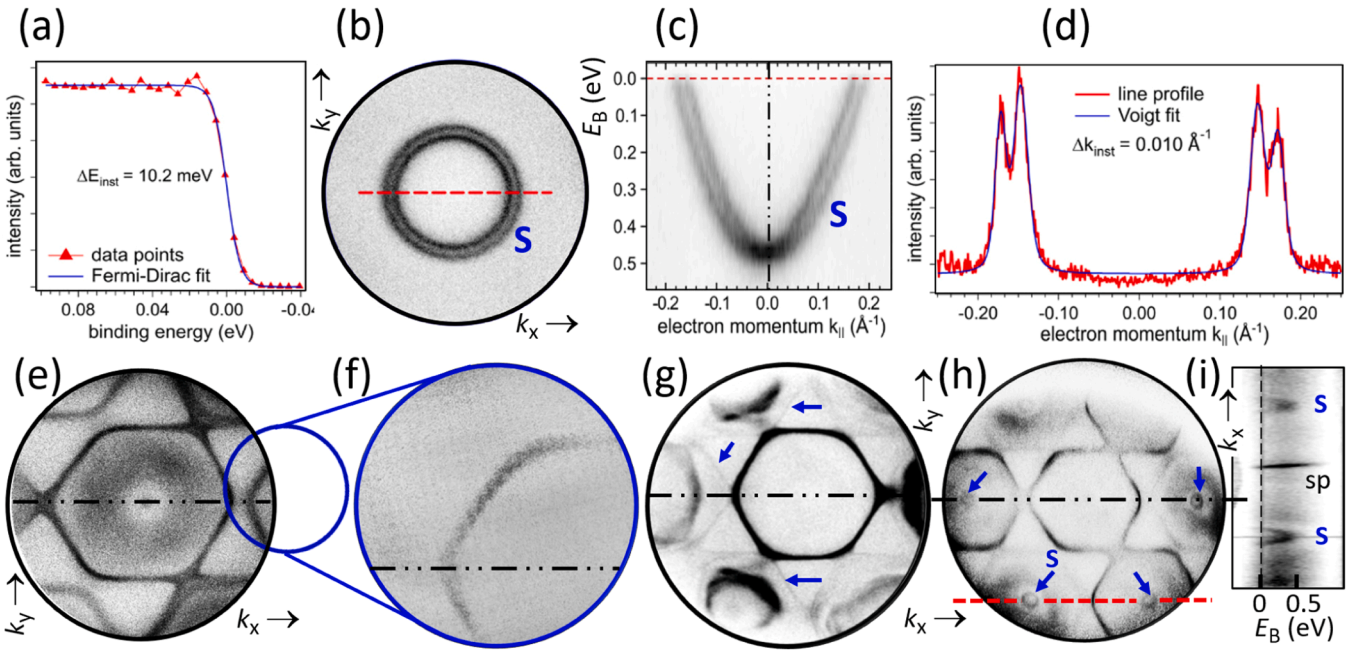

Fig. 2. (a) Fermi edge profile for a Au(111) sample measured with He I radiation (hν = 21.2 eV) at 28 K showing an energy resolution of 10.2 meV. (b) k_x-k_y map of the Shockley surface state S at E_F, and (c) its dispersion E_B-*vs*-k_x along the dashed line in (b). (d) Intensity line scan of the Rashba-split state extracted along the dashed line in (b). The blue curve is a Voigt fit showing a *k*-resolution of 0.010 Å^{-1}. (e) Fermi energy map of Au(111) recorded with synchrotron radiation at hν = 120 eV in *HSA-only mode* at E_{pass} = 30 eV. (f) Zoom in on an off-center region as marked by the blue circle in (e). (g) Fermi energy map of Cu(111) at hν = 560 eV; arrows mark faint sharp band features. (h) Fermi map of Au(111) recorded at hν = 390 eV in the *hemisphere & ToF hybrid mode* at E_{pass} = 500 eV. Arrows indicate the Shockley state observed in the second BZ. (i) Band dispersion along the dashed red line in (h) showing the Shockley state profiles and the dispersing *sp*-band. The 800 meV interval is recorded simultaneously. Here the diameter of the *k*-field of view is about 5.6 Å^{-1}.

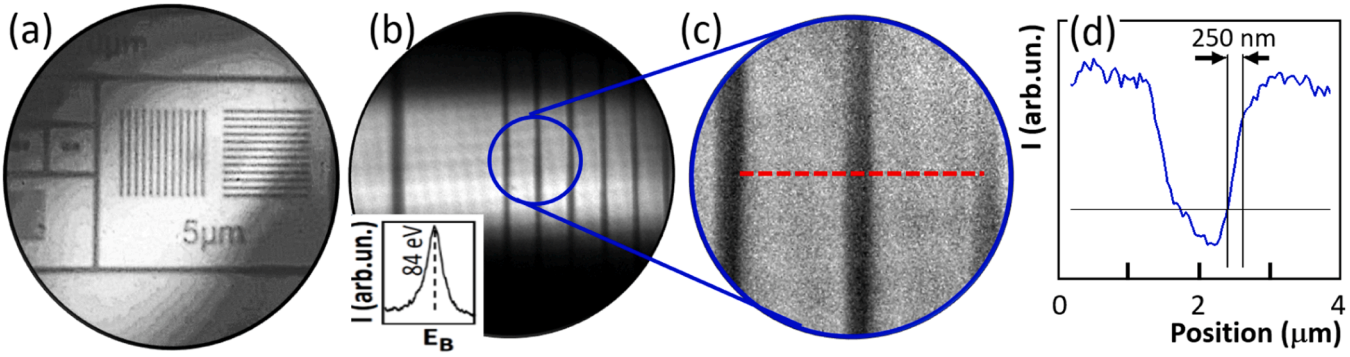

Fig. 3. Threshold PEEM image (a) and element specific X-PEEM images (b,c) of a Au / Si calibration sample with 5 µm wide stripes. PEEM image (a) shows workfunction contrast and was taken in the straight, non-energy-filtered branch using He I (21.2 eV) excitation. X-PEEM image (b) shows chemical contrast and was taken on the Au 4$f_{7/2}$ core-level signal (inset) at hν = 120 eV. (c) Zoom in on the detail as marked in (b). (d) Line profile extracted along the dashed line in (c), showing a spatial resolution of about 250 nm.

footprint of the He lamp, which is tilted by 45° with respect to the horizontal. Using a Hg lamp (hν = 4.9 eV), an identical instrument showed a spatial resolution of 40 nm [12].

For energy-filtered PEEM imaging the HSA is used. The entrance lens system of the microscope can focus a real-space (Gaussian) or momentum image onto the entrance slit of the HSA. The latter case establishes the *X-PEEM imaging mode*, first proposed in the seminal work of Tonner [18] and later demonstrated by Bauer et al. [19]. A second approach for X-PEEM imaging is to focus Gaussian images onto the analyzer slits (like in *k*-imaging), but adjust the transfer optics at the exit of the analyzer (Fig. 1(b), top branch) to focus the plane of the exit slit onto the detector. This approach was applied in Figs. 3(b,c) In both cases, an energy-filtered real-space (Gaussian) image of the sample surface is formed at the detector.

Figures 3(b,c) show energy-filtered X-PEEM images of the same test object. Here the photon energy was 120 eV and the HSA was set for the Au 4$f_{7/2}$ core-level signal; spectrum see inset of (b). These X-PEEM images show chemical contrast. The height of the bright horizontal stripe in (b) corresponds to the width of the exit slit of the HSA (here 400 µm). Inside the exit slit is a 20x magnified image of the sample. Zooming in gives the magnified detail image (c) with well resolved stripes. A line scan across one of the edges (dashed line in c) gives a spatial resolution of 250 nm, as shown in Fig. 3(d). This result is competitive with dedicated synchrotron XPEEM instruments such as the HAXPEEM [20]. The XPEEM mode is not only important for chemical imaging in real space, but also for defining the size and selecting the position of a small region of interest (ROI). By inserting a small field aperture, it is possible to select a ROI within a larger photon footprint, enabling µARPES, µXPS or µXPD. The smallest available field aperture corresponds to a nominal ROI on the sample of about 500 nm. Using a similar lens system a ROI of

900 nm has been demonstrated [21] with the photon footprint (hν = 6.4 eV) being about 30 μm.

3. The 'hemisphere & ToF' hybrid mode

3.1. Implementing the hybrid mode

For high repetition rate sources, the time T between adjacent photon pulses may be too short for pure ToF photoelectron spectroscopy. This is the case for most synchrotron sources operating at 500 MHz pulse period, and many laser sources and intra-cavity enhanced HHG sources with 60-80 MHz pulse rates [22]. In hybrid mode, the HSA acts as a pre-filter, reducing the transmitted energy band to any desired value. This energy band is then resolved by the ToF analyzer to achieve the desired resolution. The first proof of principle with the hybrid approach was performed in the Mainz laboratory using an 80 MHz UV laser [11].

The ratio of the period T to the time resolution of the detector Δt defines the number of resolvable energy slices. In the present setup T = 2 ns and Δt = 145 ps. Technically, this gives us 14 resolvable energy points. To avoid overlapping of successive electron trains the number of usable energy points is 12.

Fig. 4 shows results of the first beamtime. To understand the schematic patterns in (a,b), we recall the basics of the MM mode of operation. The electron lenses are adjusted to produce Gaussian images in the entrance and exit slits (planes GP2 and 3 in Fig. 1(b)). There, the two-dimensional momentum distribution is encoded in the angular pattern. Halfway between entrance and exit a *k*-image is located (Fourier plane FP3). The exit lens system behind the analyzer acts as a Fourier lens and focuses a momentum image onto the detector plane. Finally, the time-of-flight in the drift section resolves the energies within the transmitted band.

The transit time spread of the electrons in the analyzer due to different path lengths, cf. rays 1, 2 and 3 in Fig. 1(b), depends on the pass energy and the transversal momentum in the dispersive direction. We have chosen k_x and k_y for the non-dispersive and dispersive directions, respectively; see coordinate system in Fig. 1(b). The time spread is generally considered detrimental for time-resolved experiments with HSAs [13,14]. In an early experimental study using synchrotron radiation at Soleil (Saint-Aubin, France), Bergeard et al. [23] found a time spread of < 140 ns for a HSA with 200 mm radius at a pass energy of 2 eV. This spread appears 'random' in the standard mode of operation. However, it is 'deterministic' in momentum resolved recording. Fig. 4(a) shows a scheme of the electron distribution with the time spread along the k_y direction; τ is the time of flight of the electrons from the sample to the detector. To a good approximation, the time spread is a linear function of the entrance angle [12]. Therefore, it appears in the *k*-image as a tilt of the measured distributions on the time axis τ. In other words, the energy isosurfaces, such as the Fermi energy plane, appear tilted in the (k_x, k_y, τ) coordinate frame. When deriving the quantity of interest (k_x, k_y, E_B) from the measured raw data, the tilt is corrected by an affine transformation, leading to the result sketched in Fig. 4(b).

For the measurements in Fig. 4, the pass energy and the entrance / exit slits of the hemisphere were set to 330 eV and 500 μm, respectively. The transmitted intensity versus energy approximately corresponds to a Gaussian function with a nominal half-width defined by Eq. (1), in this case ΔE_{HSA} = 370 meV. The drift energy in the ToF section is set to 24 eV, resulting in a usable energy window of $\Delta E_{ToF} \approx 0.5$ eV, which fits into the 2 ns period of the X-ray pulses. The energy resolution of the ToF measurement is given by Eq. (1) in Ref. [11]. Here it is 59 meV, which matches the photon bandwidth for hν = 110 eV. Reducing the drift energy to 15 eV improves the energy resolution of the ToF analysis to 37 meV, but requires a reduction of ΔE_{HSA} to avoid temporal overlap at the

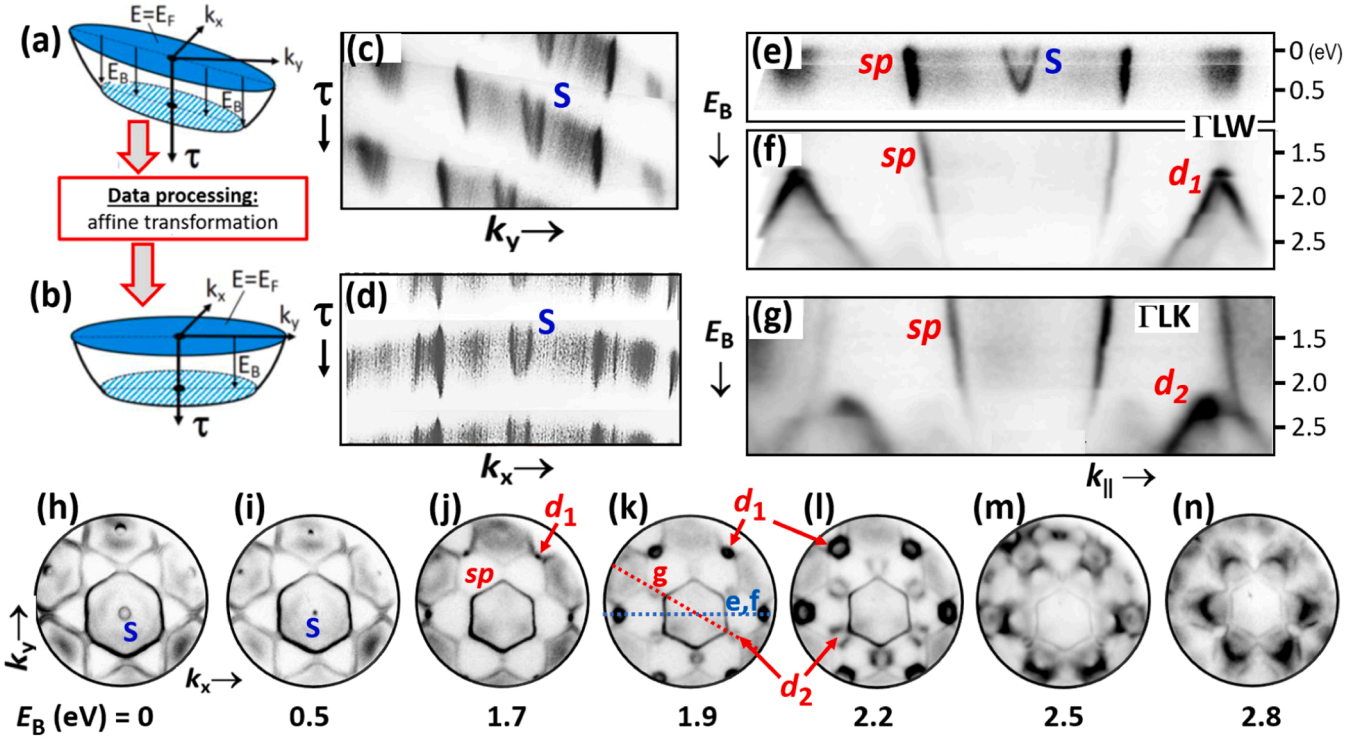

Fig. 4. First measurements with the *hemisphere + ToF hybrid mode* at beamline I09. All data were taken for a Au(111) sample at hν = 110 eV and E_{pass} = 330 eV. (a,b) Illustration of how the tilt of the patterns due to the transit time spread is numerically corrected by an affine transformation. (c,d) Raw data showing the effect of the tilt in the τ-*vs*-k_y section (c) and curvature due to fringe field effects in the τ-*vs*-k_x section (d). The Shockley state S is fully included in these sections. (e-g) Processed E_B-*vs*-$k_{||}$ sections in different azimuthal orientations as marked in (k), corresponding to the ΓLW and ΓLK planes. These sections show the *sp*-band and the Shockley state (e) and the onset of the *d*-bands d_1 (f) and d_2 (g). The patterns are patched for two (e) and four 0.3 eV wide intervals (f,g). (h-n) k_x-k_y sections at different binding energies as indicated.

boundaries of the time interval. In general, the parameters can always be adjusted so that the photon bandwidth is the limiting parameter for the energy resolution. Fig. 4(c,d) show raw data that were recorded at $h\nu = 110$ eV and $E_{pass} = 330$ eV. The unprocessed sections along the dispersive direction τ-*vs*-k_y (c) and non-dispersive direction τ-*vs*-k_x (d) show the tilt of the isoenergetic surfaces in the (k_x, k_y, τ) coordinate frame as sketched in (a). In addition, both sections show a curvature due to the α^2-term and a fringe field effect.

The Shockley state S (width ~500 meV) is fully visible in this single acquisition without scanning, confirming our expectation of a usable energy window of $\Delta E_{ToF} \approx 0.5$ eV under the given conditions. Due to the Gaussian transmission profile of the HSA, the intensity is reduced at the upper and lower limits of the time window. Fig. 4(e) shows data recorded at the same settings after the transformation described in (a) → (b). The tilt due to the transit time and the curvature due to spherical aberration and fringe field effects are corrected by the affine transform. To avoid quenching at the upper and lower ends of the energy band, we concatenated two data arrays of 300 meV width each. Now the intensity reduction at the Fermi energy and at the bottom of the Shockley state is eliminated. After the correction the Fermi energy appears horizontal in the E_B-*vs*-k_y section Fig. 4(e). An advanced operating mode is under development. This mode will scan the sample bias in small steps and stitch the time/energy slabs together. The gain factor will be the same.

Fig. 4(f) and (g) show two sections through the data stack in the region of the *d*-band onset. This stack was concatenated from 4 acquisitions with 0.3 eV steps of the sample bias. The azimuthal orientations of the band structure plots are marked in Fig. 4(k). They correspond to the planes ΓLW and ΓLK of the 3D Brillouin zone. The top of the *d*-band (band d_1) is visible in the ΓLW section parallel to the k_x-axis (Fig. 4(f)), while a cut in the ΓLK mirror plane, Fig. 4(g), shows the onset of the second *d*-band (band d_2).

Fig. 4(h-n) show k_x-k_y sections at selected binding energies as indicated below. The top and bottom of the Shockley state S are shown in (h) and (i), respectively. The onset of the top and second *d*-bands (d_1 and d_2, respectively) are shown in (j) and (k). The sections in Fig. 4(l-n) show the evolution of the *d*-band complex with increasing binding energy. An automatic correction routine is under development that will concatenate binding energy intervals with optimized matching.

3.2. Gain factor of the hybrid mode

The efficiency gain when switching from the standard 2D (k_x,k_y) to the 3D (k_x,k_y,E_{kin}) hybrid mode depends on several factors. The measurements of Fig. 4 provide a first estimate of the gain factor for the given conditions and allow an extrapolation towards higher resolution. The energy resolution of the electron detection is adapted to the photon bandwidth of 50 meV (achieved for photon energies of 110 – 150 eV). 50 meV is obtained in the *HSA-only mode* at $E_{pass} = 50$ eV. This value corresponds to 10 meV resolution measured with the He lamp at $E_{pass} = 10$ eV (Fig. 2(a)). By activating the 'ToF booster', the pass energy can be increased to $E_{pass} = 250$ eV, resulting in an energy interval of ~0.5 eV width. As discussed in 3.1, the ToF analyzer resolves this band into 12 usable energy slices of ~42 meV width.

A second contribution to the total gain occurs at the entrance aperture of the HSA. Containing a Gaussian image, the analyzer entrance aperture acts as a field aperture. At $E_{pass} = 50$ eV the entrance lens operates with a magnification factor of 20 between the sample surface and the analyzer entrance plane. This means that the 500 μm entrance aperture corresponds to an observed disk of 25 μm diameter on the sample surface. This factor was confirmed by Fig. 3(b), which shows both the 500 μm analyzer slit as a bright horizontal stripe and the 5 μm stripe pattern on the test sample, magnified by a factor of 20. According to Liouville's theorem, the magnification varies with $E_{pass}^{-1/2}$. Thus, increasing E_{pass} from 50 to 250 eV increases the accepted area on the sample by a factor of 5. This would be the transmission gain factor for a large photon footprint homogeneously illuminating the region of interest on the sample. For the given photon footprint, the image is partially cut off by the entrance aperture and we estimate a transmission gain factor of 2. Within these conservative estimates, we derive an efficiency gain factor of 12 from the number of resolved time slices and 2 from the larger accepted area on the sample, giving a total factor of 24.

We extrapolate these values to the case of higher resolution, which requires a lower pass energy and smaller slits of the HSA. Our best resolution of 4.2 meV was achieved with $E_{pass} = 8$ eV and 200 μm slits [11]. With these slits a similar resolution in the hybrid mode would be achieved with $E_{pass} = 80$ eV. Under these conditions the ToF analyzer can resolve 12 usable energy slices of 4.2 meV width. At the sample surface the 200 μm entrance aperture corresponds to a 10 μm diameter acceptance disk for $E_{pass} = 80$ eV due to the magnification factor of 20. For a typical photon footprint of ~30 μm the transmission factor would be 9 and the total gain factor about 100. These considerations apply to high-resolution beamlines at 500 MHz synchrotrons, such as I05 at Diamond [24] and several others [25–27].

A few synchrotrons such as MAX IV and PETRA III operate at 100 MHz. High-resolution beamlines at such synchrotrons (e.g. the Bloch beamline with 5 meV resolution [28]) would provide fascinating conditions, because for T = 10 ns the detector resolution of 145 ps yields ~70 resolved time slices. Together with a typical transmission factor of 2-3 (for beamlines with small photon footprints), the total gain would exceed two orders of magnitude. The conditions at 100 MHz beamlines are quite similar to those for laser-ARPES (typically 80 MHz pulse rate; T = 12 ns) [29]. The measurements in Ref. [11] were performed with an 80 MHz UV laser.

Last but not least, the time resolution is another parameter with potential for improvement. The time resolution is ultimately limited by the width of the photon pulses. For DIAMOND, the FWHM is 40 ps, which is a factor of 3.6 better than the time resolution of 145 ps measured for our delay-line detector [30]. Tremsin et al. [31] presented a comparison of different types of MCP-based time-resolved image detectors. Several types achieve resolutions in the 100 ps range or below. A time resolution of 54 ps (3σ value) has been reported in a photoelectron-photoion coincidence experiment [32]. The use of a detector with such a resolution would lead to a significant improvement in efficiency.

To conclude this section, we note that also the diameter of the recorded *k*-field increases with increasing pass energy. The limited angular filling of the HSA translates into larger parallel momentum at higher E_{pass} [12]. This effect can be seen by comparing Fig. 2(e), recorded in the *HSA-only mode* at E_{pass}= 30 eV with Fig. 2(h), measured in the *hemisphere & ToF hybrid mode* at E_{pass}= 500 eV. In the latter case the visible area in *k*-space is increased by a factor of 3. This larger area is particularly advantageous for photoelectron diffraction studies, since a larger number of Kikuchi bands can be observed (cf. Sec. 4.4).

4. Momentum-space imaging

4.1. Band mapping of a 2D system

One of the key features of this instrument is the improved detection efficiency. Even in the *HSA-only mode* the parallel acquisition of (k_x,k_y)-arrays for the entire BZ at a given kinetic energy allows a much faster investigation of e.g. two-dimensional electron systems. Such studies suffer especially from low count rates and thus long exposure times. As an example, Fig. 5 shows measurements of bilayer graphene on SiC.

The sample was heated to 200°C after insertion into the vacuum system and then cooled down to 28 K. The beamline was set to 150 eV photon energy, resulting in high surface sensitivity and an overall energy resolution of about 50 meV. With the mirrors optimized for a best focused beam, the spot size on the sample was about 20 × 50 μm. The

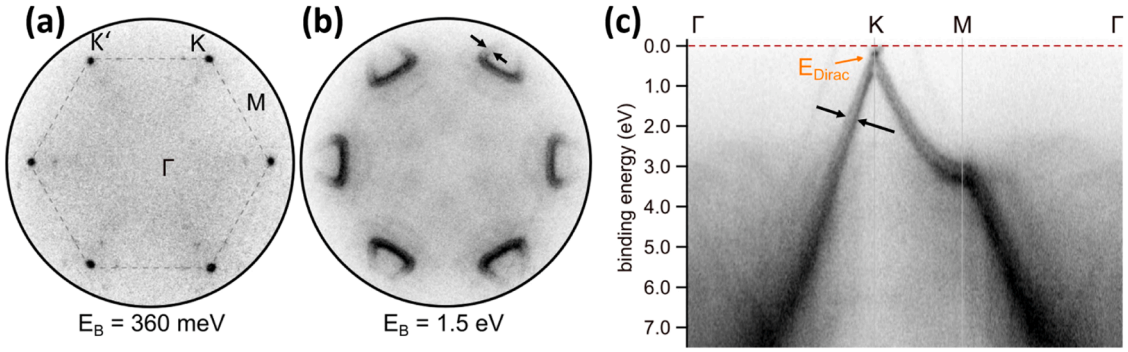

Fig. 5. Band mapping of a graphene bilayer on SiC at a photon energy of 150 eV (bandwidth 50 meV). (a,b) k_x-k_y momentum maps recorded at binding energies of 360 meV and 1.5 eV, respectively. The Dirac point appears significantly below E_F (a); arrows denote the split Dirac band (b). (c) Band dispersion E_B-vs-$k_{||}$ along the Γ-K-M-Γ direction; arrows denote the band splitting characteristic for the bilayer.

electron lenses were set for the *k*-field of view to cover a full BZ. This measurement was performed in the HSA-only mode with a pass energy of 30 eV. The 3D data array (k_x,k_y,E_B) was acquired by scanning the voltage applied to the sample in steps of 20 mV and recording a (k_x,k_y)-pattern at each energy. All patterns were then concatenated to form the final 3D array.

Fig. 5(a) and (b) show two constant energy maps measured at different binding energies. *k*-image (a) shows the hexagonal arrangement of the Dirac points at a binding energy of 360 meV. The additional faint structures (and also the faint satellite bands in Fig. 5(c)) result from multiple scattering of the photoelectron wave at the non-commensurate SiC and graphene lattices and the associated umklapp processes. The *k*-pattern at the higher binding energy of 1.5 eV in Fig. 5(b) shows the expected outward dispersion of the Dirac bands [33,34]. Closer inspection reveals a recurring two-band structure (see arrows in (b,c)) that is characteristic for the graphene bilayer. This two-band structure is most clearly seen in the E_B-vs-$k_{||}$ section of Fig. 5(c), which shows the band dispersion along the Γ-K-M-Γ direction.

4.2. Mapping of the circular dichroism texture

Circular dichroism measures the different response of a system to photon beams of the opposite helicities. In valence band photoemission, it originates from a matrix element effect in the excitation step. CD-ARPES is a sensitive probe of wavefunctions and provides specific information about topological systems [35,36]. This effect has been termed circular dichroism in the angular distribution (CDAD) and it can be described by two quantities: The *CDAD signal* is the difference of the intensities recorded with the two photon helicities I_{RCP} - I_{LCP}; the *CDAD asymmetry* is defined as the relative quantity $(I_{RCP} - I_{LCP})/(I_{RCP} + I_{LCP})$. To demonstrate the information content of CD-ARPES, two examples are shown: Here the atomic monolayer system indenene and in 4.3 gold and copper as prototypical bulk metals with simple *sp* valence bands.

Fig. 6 shows an example of CDAD for the valence band of graphene-intercalated indenene, i.e., a monolayer of In atoms sandwiched between a SiC(0001) substrate and a monolayer of graphene. Indenene has been shown to be a two-dimensional quantum spin Hall insulator [37], with the graphene capping acting as an efficient protection against environmental degradation [38]. CDAD provides information on the orbital angular momentum and hence the Berry curvature in the band structure of this topological insulator [39]. Fig. 6(a,b) show the momentum patterns measured with right and left circularly polarized light (RCP, LCP) at a photon energy of 230 eV.

The graphene K-points of the capping layer are clearly visible (arrows in (a)) and are superimposed on the In 5*p* bands. A pronounced dichroism contrast from top to bottom is visible, which reverses when the photon helicity is switched (cf. (a) and (b)). The circular dichroism is quantified in (c) as the difference signal and in (d) as asymmetry, shown in blue and red for positive and negative asymmetry. The CDAD asymmetry reaches almost 100% and shows a textbook-like antisymmetry with respect to the horizontal mirror plane running through the center (dashed lines). Note that the use of soft X-ray photoemission with its enhanced probing depth has allowed us to probe the indenene band structure through its graphene capping, i.e., in a device-like geometry. This demonstrates the high potential of this momentum microscope for *in-operando* spectroscopy of functional nanostructures.

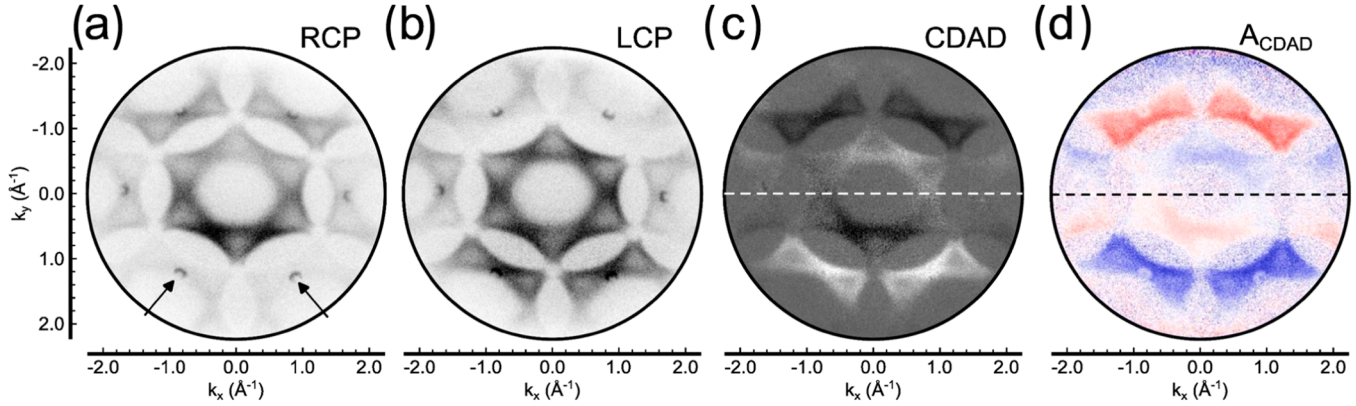

Fig. 6. CDAD for the valence band of indenene intercalated into the graphene / SiC interface. (a,b) Constant energy maps measured at a photon energy of 230 eV with right and left circularly polarized light, respectively. (c) Resulting CDAD in grey scale and (d) CDAD asymmetry on a color scale showing that the circular dichroism is antisymmetric with the direction of photon incidence (mirror axis denoted as dashed line).

4.3. Mapping energy surfaces and circular dichroism in 3D k-space

With photon energies up to 2 keV, the soft X-ray branch of beamline I09 is ideally suited to probe not only surface states and adsorbates, but also the bulk electronic structure. The inelastic mean free path (IMFP) of photoelectrons in Cu and Au studied below is as low as 0.5 nm for both at 110 eV and increases to 2.9 and 2.1 nm, respectively, at 2 keV [40]. The lower end of the energy range is close to the minimum of the universal curve providing high surface sensitivity. Photon energies towards the upper end provide access to bulk electronic structures of 3D systems. Such data are of interest, e.g., in the context of transport properties. In addition, the large IMFP allows the study of buried interfaces, samples with protective coatings and deeper layers.

A central application of soft X-ray MM is the mapping of electronic band structures in 3D *k*-space, an efficient way to perform ARPES. Here we show how full-field imaging MM is used to image isoenergetic surfaces in *k*-space, including their circular dichroism texture (CD-ARPES). By looking directly into momentum space, we obtain *k*-patterns without the need to transform the data from real-space polar coordinates to *k*-space coordinates.

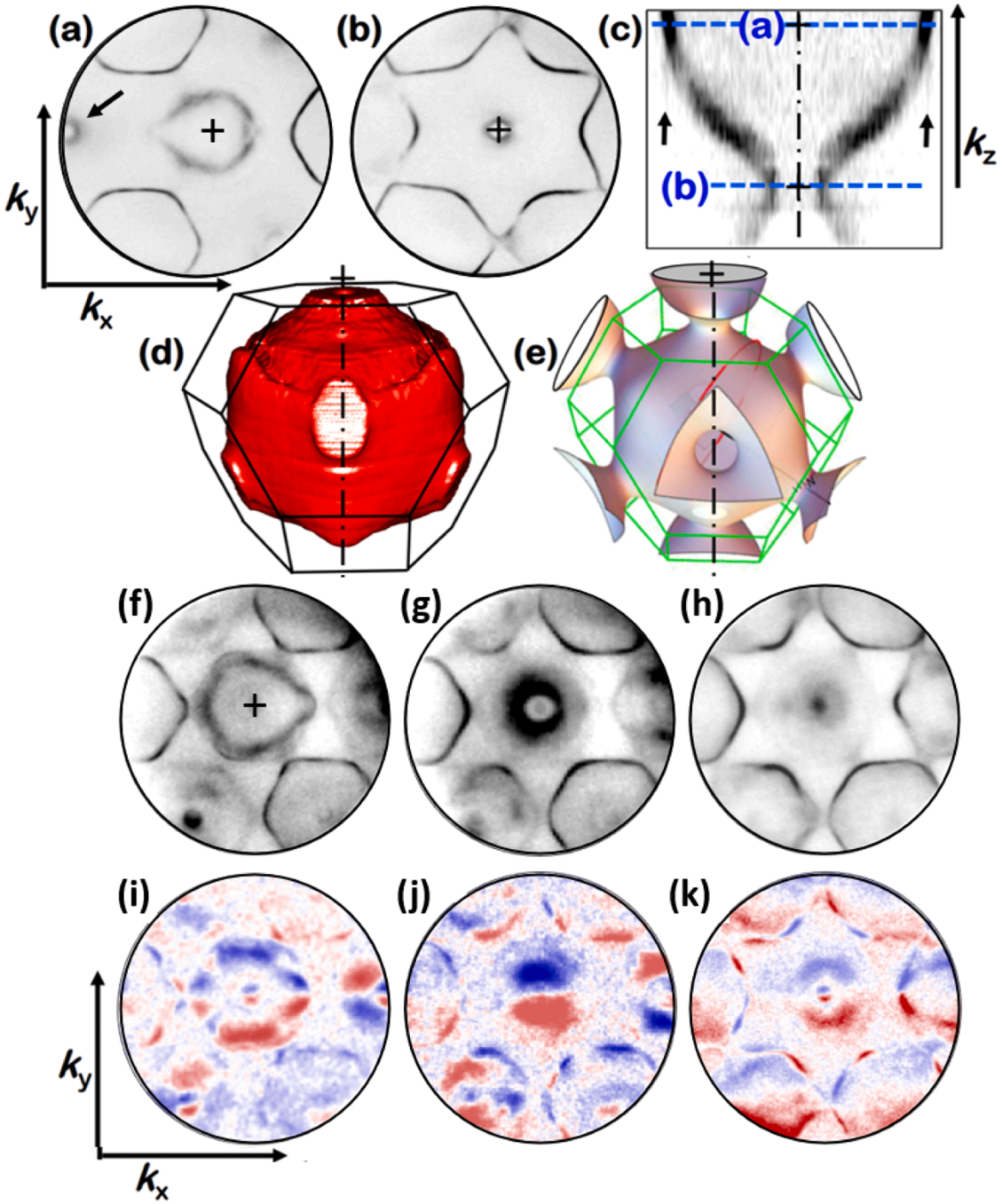

Fig. 7. Mapping of energy surfaces and circular dichroism texture in 4D (k, E_B) parameter space. (a,b) k_x-k_y momentum images for Cu(111) at the Fermi energy for photon energies of 630 and 690 eV, respectively, corresponding to different k_z. (c) k_x-k_z section through the 3D data array, concatenated from 20 images as in (a,b) in the photon energy range from 520 to 720 eV. This plot shows only the innermost band, centered around the + signs in (a,b). (d) View of the experimental Fermi surface of Cu, derived from the concatenated data stack. (e) Fermi surface of Cu as derived from dHvA measurements (from [43]). (f, g and h) Examples of k_x-k_y images at the Fermi level and (i, j and k) corresponding CDAD texture of the *sp*-band of Au(111) taken at hν = 280 eV (f,i), 300 eV (g,j) and 320 eV (h,k).

As an example, Fig. 7 shows the mapping of the Fermi surface of Cu. The transversal coordinates k_x and k_y are directly accessible in the images, while the coordinate k_z is varied by changing the photon energy. The topology of the Cu Fermi surface is deduced from de Haas – van Alphen (dHvA) experiments. We adopt the terminology of dHvA measurements, as introduced in the seminal work of Shoenberg [41,42]. Fig. 7(a,b) show k_x-k_y patterns at photon energies of 630 and 690 eV. The Fermi surface section Fig. 7(a) lies halfway between the *extremal dHvA orbits*, the 'belly orbit' at 560 eV (Fig. 2(g)) and the 'neck orbit' in Fig. 7(b). The full 3D Fermi surface was then concatenated from 20 such k_x-k_y patterns, each taken at a different photon energy between 520 and 720 eV with a 20 minute dwell time. Fig. 7(c) shows a k_x-k_z section through the concatenated stack in the region between the belly and the neck. The arrow in (a) denotes the neck orbit in the adjacent 2nd BZ. Fig. 7(d) shows a 3D view of the experimental Fermi surface, truncated at the boundaries of the 1st BZ. This Fermi surface is qualitatively similar to the Fermi surface derived from the dHvA measurements shown in Fig. 7(e) (from Ref. [43]).

A close inspection of Fig. 7(a) and (f) reveals that the band contour centered around + appears diffuse or even split. Furthermore, the belly contour is visible as faint lines in many k_x-k_y images, regardless of k_z, see the arrows in Fig. 2(g). These observations point to non-free-electron-like final states and resemble the multiple-final-states signature described in Ref. [17]. These authors found signatures of several coexisting final states that interfere with each other for Ag. These effects are visible as distortions in the upper part of our experimental Fermi surface, Fig. 7(d). One could also attribute the faint lines in Fig. 2(g) to a kind of 'density-of-states effect' in the *k*-space mapping. The high density of states corresponding to the extremal orbits observed in the dHvA measurements could lead to weak photoemission signals, even when k_z does not 'formally' intersect the correct plane of the Fermi surface in the photoemission transition. Another possibility is the occurrence of surface resonances associated with surface-projected bulk states. These phenomena will be investigated in more detail alongside photoemission calculations.

Fig. 7(f-k) show examples of k_x-k_y momentum images and corresponding CDAD patterns for the *sp* valence band of Au(111). Four-dimensional ($\boldsymbol{k}$, E_B) data arrays have been recorded for both photon helicities RCP and LCP. Due to the larger lattice constant of Au, its BZ is smaller. Therefore, the momentum microscope captures a larger fraction of the neighboring BZs for Au (f-h) than for Cu (a,b). By adding the data stacks (I_{RCP}+I_{LCP}), we obtain the intensity arrays with dichroism effects eliminated. The voxel-by-voxel determination of the CDAD asymmetry (I_{RCP} - I_{LCP})/(I_{RCP} + I_{LCP}) yields the 4D texture of the circular dichroism A_{CDAD} ($\boldsymbol{k}$, E_B). Its symmetry properties are discussed in detail in Ref. [44]. The CDAD also shows antisymmetry with respect to the mirror planes perpendicular to the k_z axis.

Fig. 7(f-h) show the k_x-k_y intensity maps and Fig. 7(i-k) the corresponding CDAD patterns, taken at photon energies of 280, 300 and 320 eV. The k_z values correspond to the region between the belly and the neck of the Fermi surface, which is the region where the irregularities in the upper part of Fig. 7(d) occurred. Throughout the *k*-field, the CDAD shows a rich structure that varies strongly with photon energy. Fig. 7(h) is near the neck and its prominent feature is a sixfold 'star' formed by the 'belly' contours of the second BZs. In the CDAD this 'star' appears with a distinct red-blue texture. Remarkably, the diffuse intensity background outside of the band features also shows a strong dichroism with a pronounced texture. This effect is much stronger for Au than for Cu (data not shown here). The much richer and finer grained structure of the CDAD patterns allows for more accurate structural information in the probed volume. Details are beyond the scope of this article and will be published in a separate paper. Photoemission calculations will shed light on this phenomenon. Finally, we note that a detailed discussion of the CDAD of the Au(111) Shockley state can be found in Ref. [45].

4.4. Full-field photoelectron diffraction

Parallel imaging of large *k*-fields of view allows a new, highly efficient approach to photoelectron diffraction (PED; also known as XPD in the X-ray range). Such measurements require high angular resolution; our instrument achieves 0.03°. The energy resolution is usually determined by the photon bandwidth. PED measurements thus take full advantage of the capabilities of the momentum microscope. Full-field diffractograms show complex patterns of intersecting Kikuchi bands [46]. PED analysis can be combined with valence band mapping under identical conditions (lens settings, photon footprint, ROI on the sample) by simply tuning from the core-level signals to the valence band. The combination of PED and valence-band mapping in a single experiment provides access to the interplay of geometric and electronic structures, e.g., when crossing a structural phase transition. Full-field imaging PED is particularly attractive because of its unprecedented acquisition speed. For intense core levels, such diffractograms can be viewed in real time at a frame rate of 1 Hz.

As an example, Fig. 8 shows a series of diffractograms for the 3*d* and 3*p* core levels of a Ge(001) crystal. The series covers the energy range from near the minimum of the IMFP curve to the bulk sensitive regime. The diffraction kinematics is determined by the final state of the photoelectrons *inside* the material $E_{final} = h\nu - E_B + V_0$, where E_B is the binding energy of the core level and V_0 is the inner potential. Between $E_{final} = 106$ and 1036 eV (Fig. 8(a-e)) the IMFP of Ge increases from 0.5 nm to 2.2 nm [40]. All patterns are rich in detail even at kinetic energies as low as 106 and 172 eV (a,b). This is surprising and systematic calculations will clarify the reason for the rich structure of the patterns in the first row. We see clear boundaries of the central Kikuchi band, dashed lines in (c), and the rhombic shaped feature with upper left and lower right edges marked by arrows in (a,f). The magnification of the *k*-images varies with E_{kin}, so the 106 eV pattern (a) appears magnified compared to the 1036 eV pattern (e,f). The fine structure of the central region shows a strong energy dependence, sequence (a-e).

The conventional framework for analyzing photoelectron diffraction patterns is in real-space polar coordinates [47], whereas our instrument captures PED patterns on a momentum scale. At X-ray energies the diffractograms are dominated by Kikuchi bands [48], which contain both, *k*-space and real-space information. The widths of the Kikuchi bands correspond to multiples of reciprocal lattice vectors, thus providing a *metric for the k-space coordinates* [49]. On the other hand, the midlines and intersection points of bands correspond to projected *lattice planes and atom rows* along the high-symmetry directions of the crystal in real space. The filigree fine structure of PED in the X-ray region results from the short electron wavelength combined with the large IMFP. In the keV range, 10^5 to 10^6 atoms contribute to the diffraction process. This is the classical *Kikuchi regime* as perfectly understood in electron microscopy [50]. At high energies we obtain true bulk information because the surface contribution is negligible. Multi-beam dynamical Kikuchi band theory using the Bloch wave approach [51] gives excellent agreement with experiments (for a review see [52]).

Fig 8(f,h) show calculations using the Bloch wave approach. Comparison of (f) with the measurement (e) shows reasonable agreement both in the appearance of the Kikuchi band marked by dashed lines and in the fine structure in the central region. The simulation in (h) shows a larger *k*-field, illustrating how the complex central pattern arises from many crossing Kikuchi bands. The dashed ellipse indicates the region of the measured pattern (g).

At $h\nu = 1050$ eV the Ge 3*d* and 3*p* patterns ($E_{final} = 1036$ and 944 eV, respectively) show a significant CDAD, as demonstrated in Fig. 8(i,j). The origin of this effect has been discussed in Ref. [53]. The CDAD requires a non-coplanar geometry of the helicity vector of the incident photon beam, the photoelectron momentum and the electronic quantization axis, here the surface normal [54]. As a consequence of this symmetry property, the CDAD vanishes in the horizontal mirror plane and the regions above and below the mirror plane show an

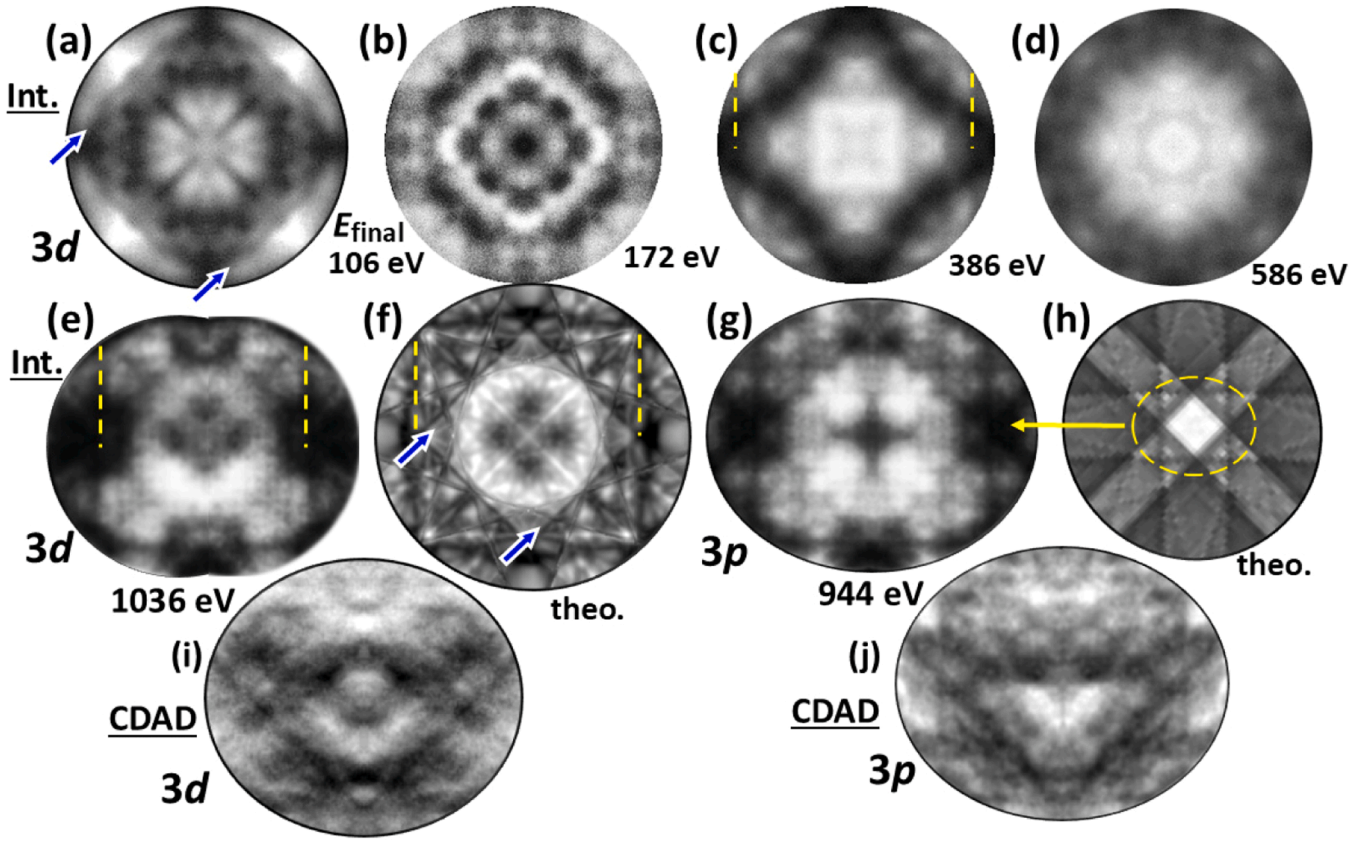

Fig. 8. Photoelectron diffraction and circular dichroism in 3*d* and 3*p* core-level photoemission from a Ge(001) sample. (a-e) k_x-k_y momentum images for Ge 3*d* at different final state energies as indicated in the panels. (f) Calculated diffractogram for E_{final} = 1036 eV, corresponding to the measured pattern (e). The arrows in (f) and (a) mark the same diamond feature. (g) The same for the Ge 3*p* core level at E_{final} = 944 eV. (h) Calculated pattern with a larger diameter; the dashed ellipse marks the size of (g). Bottom row: Measured circular dichroism texture for Ge 3*d* (i) and 3*p* (j), corresponding to the intensity patterns in (e) and (g). Here the diameter of the *k*-field is about 6 Å^{-1}.

anti-symmetric CDAD. The dichroism texture is very different from the corresponding intensity patterns, as we compare with Fig. 8(e,i) for Ge 3*d* and Fig. 8(g,j) for Ge 3*p*. CDAD is a matrix element effect and results from the local excitation at the emitter atom. However, the Kikuchi diffraction process strongly modifies the CDAD, leading to complex asymmetry patterns. First calculations using a layered multiple scattering approach show reasonable agreement with experiments [55,56].

In the 100 eV range, PED has been used to analyze surface relaxation, reconstruction and adsorbate structures, in particular adsorption sites (see, e.g., review articles [57,58]). Due to the short IMFP the nearest neighbor atoms contribute dominantly to the scattering processes. This regime is commonly referred to as the *holographic regime* because it is possible to retrieve the real-space atomic configuration from the diffraction pattern [59,60]. Full-field imaging PED at low energies has so far only been performed with the HEXTOF momentum microscope at the free-electron laser FLASH [61]. A related type of structural information has been obtained with the same instrument by imaging the *k*-pattern of photoelectrons from molecular orbitals, termed orbital tomography [62].

In addition to the ability to perform detailed structural analysis, PED patterns also have practical aspects: they provide an alternative metric for *k*-space and show distinct directions in real space, e.g. the azimuthal orientation and the exact position of the sample surface (important for samples with different domains). This allows for quick alignment of sample and microscope settings.

5. Summary and outlook

A novel photoelectron momentum microscope installed at the soft X-ray branch of beamline I09 of the Diamond Light Source was presented. The instrument's primary component is a large hemispherical spectrometer, accompanied by a time-of-flight (ToF) analyzer positioned behind the exit slit. The beamline covers a photon energy range from 105 eV to 2 keV, allowing both surface and bulk sensitive ARPES measurements. Circular polarization is available at hν > 145 eV to record circular dichroism in the photoelectron angular distribution (CDAD). The momentum microscope is integrated into a versatile sample handling and preparation system, including equipment for surface preparation and analysis (sputtering, annealing, LEED).

An energy resolution of the HSA of 4.2 meV FWHM has been achieved with small analyzer slits (200 μm) and E_{pass} = 8 eV [12]. Under conditions conducive to synchrotron experimentation (400 μm slits and E_{pass}= 10 eV), a width of 10.2 meV FWHM was obtained. A momentum resolution of 0.010 Å^{-1} was validated for the Au Shockley state. The large angular filling of the entrance lens and the hemispherical analyzer (HSA) facilitate the imaging of *k*-fields with a diameter greater than 6 Å^{-1}. A focused and monochromatized He lamp is utilized for off-line measurements at hν = 21.2 eV (He I) and 40.8 eV (He II). This lamp was used for the resolution measurements.

The instrument is capable of operation in two different modes: The *HSA-only mode,* without ToF analysis, facilitates 2D recording (k_x,k_y), akin to single and double hemisphere momentum microscopes at other synchrotron sources [3–7]. Different energies are measured sequentially. In the *hemisphere & ToF hybrid mode,* the HSA functions as a bandpass pre-filter for the ToF analyzer. This combination allows efficient 3D (k_x,k_y,E_{kin}) ToF momentum microscopy at 500-MHz synchrotrons, despite the short period of 2 ns. With a time resolution of 145 ps, the detector simultaneously resolves 12 usable time slices in the 2 ns

time interval. The α^2-term and the transit time spread resulting from different path lengths in the HSA are corrected numerically.

The innovative approach integrates two different energy discrimination schemes: energy dispersive in the HSA and time dispersive in the ToF analyzer. In a comparative study, Maklar et al. [63] evaluated these two approaches using separate instruments in the same setup. Their analysis demonstrates the complementary nature of the two spectrometers, especially for time-resolved ARPES experiments. We note that the hemispherical analyzer utilized in the study [63] was a standard ARPES analyzer. It records $I(E_B,k_x)$ patterns as a function of binding energy E_B and parallel momentum k_x, rather than momentum images $I(k_x,k_y)$.

In addition to *k*-space imaging, we have demonstrated the potential of energy-filtered real-space imaging (X-PEEM) for fast chemical nanoanalysis. Instead of a momentum image, a Gaussian image is focused on the detector. Initial experiments with a lithographic test sample demonstrated a lateral resolution of 250 nm for chemical imaging at the core-level signal of Au 4*f*. In this context a point of general interest is the ability of the instrument to study small samples with sizes down to a few micrometers. Two cases have to be distinguished: Small flakes of 2D materials on flat substrates can be selected by closing the field aperture in the intermediate image (Fig. 1(b)) to the desired size. Small cleaved 3D crystals would deform the electric field at the sample surface. We are currently installing a new type of front lens that can significantly reduce the electric field at the sample. This greatly reduces the effect of field distortion and mitigates the risk of flashovers [64,65].

The efficiency gain from activating the ToF analyzer was estimated for a resolution of 50 meV, which is determined by the photon bandwidth of the beamline. In hybrid mode, the ToF analyzer achieves the desired resolution, enabling the HSA to operate at much higher pass energy. At E_{pass}= 330 eV, the HSA transmits a usable energy window of 0.5 eV, fitting into the 2 ns period of the X-ray pulses. The HSA's transmission profile is approximately Gaussian; therefore, temporal crosstalk can occur with the signals of neighboring photon pulses at the boundaries of the interval. Under current conditions, a number of N=12 energy slices can be used. In addition to this factor of 12 resulting from parallel energy recording, the HSA's entrance lens has a higher transmission at higher E_{pass}, which contributes to the efficiency gain. This factor depends on the size of the photon footprint in relation to the accepted area on the sample surface. The accepted area depends on the entrance aperture of the HSA and the magnification of the entrance lens. With our current parameters, this factor is 2, resulting in a total gain of approximately 24. The high recording efficiency of this instrument at beamline I09 was recently exploited in a series of measurements on the Kagome metal CsV_3Sb_5 [66].

Applications are demonstrated with typical examples. Surface sensitive ARPES for bilayer graphene on SiC at $h\nu = 150$ eV shows faint details due to the recurring two-band structure characteristic for this system. CD-ARPES using circularly polarized soft X-rays at $h\nu = 230$ eV was performed for the quantum spin Hall insulator indenene intercalated at the graphene / SiC interface. The three-dimensional band structure and CDAD texture of the valence bands of copper and gold were measured in the photon energy range between 520 and 720 eV. Surprisingly, these results for two prototypical *sp*-band bulk metals revealed unexpected details that need to be elucidated by ongoing experiments and theoretical calculations.

The large *k*-field of view is favorable for recording photoelectron diffraction (PED) patterns and their circular dichroism texture. This is shown by results for Ge 3*p* and 3*d* core levels at energies between 106 and 1036 eV. Even though the inelastic mean free path is small at low kinetic energies, the PED patterns show a rich fine structure that varies strongly with kinetic energy. Calculations of full-field imaging photoelectron diffractograms at low kinetic energies in the 100-eV range are highly desirable. In the future, a modified front lens will reduce the accelerating field at the sample surface and provide access to even larger *k*-fields [64,65].

For the hybrid microscope in its current state, we have extrapolated the efficiency gain to high-resolution beamlines at 500 MHz synchrotrons [24–27]. For 4.2 meV resolution, which was achieved in the *HSA-only mode* [11], a gain factor of about 100 is expected for beamlines with a few meV resolution. At 100 MHz synchrotrons like MAX IV (e.g., beamline [28]) and PETRA III, gain factors exceeding two orders of magnitude can be reached. Then, the current ToF resolution of 145 ps can yield ~70 resolved time slices in the 10 ns interval. These conditions are similar to those for laser ARPES (typically at 80 MHz pulse rate).

There are several ways to improve the detector. MCP-based time-resolved image detectors can achieve resolutions of better than 100 ps, see the comparison in Ref. [31]. Detectors with up to three times higher resolution (e.g. [32]) would provide a threefold gain. Additionally, pixelated solid-state detectors will soon reach a level of development useful for the hybrid microscope. Another possibility for improvement that has not yet been explored is the fast gating of the detector. This approach has been successfully demonstrated [67] with a simple ToF spectrometer at the Advanced Light Source (Berkeley) operating at 500 MHz. In a high-resolution pulsed field ionization experiment, gating of the ToF peak resulted in almost complete suppression of unwanted background electrons from nearby autoionizing features. In our setup, such a scheme could suppress the overlap of adjacent electron trains. Finally, the diameter of the recorded *k*-field increases due to the higher pass energy, e.g. by a factor of 3 in the example Fig. 2(e) and (h).

With its unique ability to perform massive parallel *k*-space mapping at a competitively high energy resolution, our hybrid momentum microscope is the next generation of photoemission instrumentation. Using it with soft X-ray excitation and the concomitant higher photoelectron mean free path allows for high-precision 3D bulk band mapping. It also provides access to buried interfaces and nanostructures, as well as facilitating in-operando spectroscopy of real devices. Furthermore, when combined with linear and circular dichroism, momentum microscopy has the potential to advance photoemission from a mere spectroscopy of energy eigenvalues into the tomography of the associated wave functions. In other words, it can provide complete information on the complex Bloch eigenfunctions and all related quantum properties, such as Berry curvature or the quantum geometric tensor. Finally, our momentum microscope is ideally suited for combination with 2D spin filtering to achieve a full quantum measurement of the band structure, a goal we plan to pursue in future work.

CRediT authorship contribution statement

Matthias Schmitt: Investigation. **Deepnarayan Biswas:** Investigation. **Olena Tkach:** Investigation. **Olena Fedchenko:** Investigation. **Jieyi Liu:** Investigation. **Hans-Joachim Elmers:** Investigation. **Michael Sing:** Investigation. **Ralph Claessen:** Investigation. **Tien-Lin Lee:** Investigation. **Gerd Schönhense:** Investigation.

Declaration of competing interest

The authors declare that they have no known competing financial interests or personal relationships that could have appeared to influence the work reported in this paper.

Acknowledgments

We thank the Diamond Light Source for providing beamtime. Sincere thanks go to Dave McCue for excellent system design and valuable technical support. We thank Aimo Winkelmann (U Krakóv) for support with the PED simulations, Surface Concept GmbH (Mainz) for support with the delayline detector, Phil King (U St Andrews) for the bilayer graphene, Jonas Erhardt and Cedric Schmitt (both at U Würzburg) for the graphene-intercalated indenene samples, and Simon Moser (U Würzburg) for helpful discussions on the circular dichroism. This work was funded by Deutsche Forschungsgemeinschaft DFG through projects CL 124/16-1, SCHO 341/16-1 and the Würzburg-Dresden Cluster of

Excellence on Complexity and Topology in Quantum Matter 'ct.qmat' (EXC2147, project ID 390858490). Further support was also provided by Diamond.

We are sad to say goodbye to Takanori Koshikawa, who for decades was one of the promoters of our field of research far beyond Japan's borders.

Data availability

Data will be made available on request.

References

[1] C. Tusche, Y.-J. Chen, C.M. Schneider, Low-energy spin-polarized electrons: their role in surface physics, Frontiers Phys. 12 (2024) 1349529, https://doi.org/10.3389/fphy.2024.1349529.
[2] G. Schönhense, H.-J. Elmers, Spin- and time-resolved photoelectron spectroscopy and diffraction studies using time-of-flight momentum microscopes, J. Vac. Sci. Techn. A 40 (2022) 020802, https://doi.org/10.1116/6.0001500.
[3] B. Krömker, M. Escher, D. Funnemann, D. Hartung, H. Engelhard, J. Kirschner, Development of a momentum microscope for time resolved band structure imaging, Rev. Sci. Instrum. 79 (2008) 053702, https://doi.org/10.1063/1.2918133.
[4] C. Tusche, A. Krasyuk, J. Kirschner, Spin resolved bandstructure imaging with a high resolution momentum microscope, Ultramicrosc 159 (2015) 520, https://doi.org/10.1016/j.ultramic.2015.03.020.
[5] F. Matsui, K. Hagiwara, E. Nakamura, T. Yano, H. Matsuda, Y. Okano, S. Kera, E. Hashimoto, S. Koh, K. Ueno, T. Kobayashi, E. Iwamoto, K. Sakamoto, S.-I. Tanaka, S. Suga, Soft x-ray photoelectron momentum microscope for multimodal valence band stereography, Rev. Sci. Instrum. 94 (2023) 083701, https://doi.org/10.1063/5.0154156.
[6] T.-H. Chuang, C.-C. Hsu, W.-S. Chiu, J.-S. Jhuang, I.-C. Yeh, R.-S. Chen, S. Gwo, D.-H. Wie, Performance of a photoelectron momentum microscope in direct- and momentum-space imaging with ultraviolet photon sources, J. Synchr. Radiat. 31 (2024) 195, https://doi.org/10.1107/S160057752300976.
[7] K. Yaji, S. Tsuda, Visualization of spin-polarized electronic states by imaging-type spin-resolved photoemission microscopy, Sci. Technol. Adv. Mater.: Methods 4 (2024) 2328206, https://doi.org/10.1080/27660400.2024.2328206.
[8] K. Medjanik, O. Fedchenko, S. Chernov, D. Kutnyakhov, M. Ellguth, A. Oelsner, B. Schönhense, T.R.F. Peixoto, P. Lutz, C.-H. Min, F. Reinert, S. Däster, Y. Acremann, J. Viefhaus, W. Wurth, H.J. Elmers, G. Schönhense, Direct 3D mapping of the fermi surface and fermi velocity, Nat. Mater. 16 (2017) 615, https://doi.org/10.1038/nmat4875.
[9] K. Medjanik, S.V. Babenkov, S. Chernov, D. Vasilyev, B. Schönhense, C. Schlueter, A. Gloskowskii, Yu. Matveyev, W. Drube, H.J. Elmers, G. Schönhense, Progress in HAXPES performance combining full-field k-imaging with time-of-flight recording, J. Synchr. Radiat. 26 (2019) 1996–2012, https://doi.org/10.1107/S1600577519012773.
[10] M. Schmitt, O. Kirilmaz, S. Chernov, S. Babenkov, D. Vasilyev, O. Fedchenko, K. Medjanik, Yu. Matveyev, A. Gloskovskii, C. Schlueter, A. Winkelmann, L. Dudy, H.J. Elmers, G. Schönhense, M. Sing, R. Claessen, Bulk spin polarization of magnetite from spin-resolved hard X-ray photoelectron spectroscopy, Phys. Rev. B 104 (2021) 045129.
[11] G. Schönhense, K. Medjanik, O. Fedchenko, A. Zymaková, S. Chernov, D. Kutnyakhov, D. Vasilyev, S. Babenkov, H.J. Elmers, P. Baumgärtel, P. Goslawski, G. Öhrwall, T. Grunske, T. Kauerhof, K. von Volkmann, M. Kallmayer, M. Ellguth, A. Oelsner, Time-of-flight photoelectron momentum microscopy with 80-500 MHz photon sources: electron-optical pulse picker or bandpass pre-filter, J. Synchr. Radiat. 28 (2021) 1891, https://doi.org/10.1107/S1600577521010511.
[12] G. Schönhense, S. Babenkov, D. Vasilyev, H.-J. Elmers, K. Medjanik, Single-hemisphere photoelectron momentum microscope with time-of-flight recording, Rev. Sci. Instrum. 91 (2020) 123110, https://doi.org/10.1063/5.0024074.
[13] R.E. Imhof, A. Adams, G.C. King, Energy and time resolution of the 180° hemispherical electrostatic analyzer, J. Phys. E: Sci. Instrum. 9 (1976) 138–142.
[14] O. Sise, T.J.M. Zouros, Position, energy, and transit time distributions in a hemispherical deflector analyzer with position sensitive detector, J. Spectrosc. 2015 (2015) 153513, https://doi.org/10.1155/2015/153513.
[15] C. Tusche, Y.-J. Chen, C.M. Schneider, J. Kirschner, Imaging properties of hemispherical electrostatic energy analyzers for high resolution momentum microscopy, Ultramicroscopy 206 (2019) 112815.
[16] T.-L. Lee, D.A. Duncan, A two-color beamline for electron spectroscopies at diamond light source, Synchr. Radiat. News 31 (2018) 16, https://doi.org/10.1080/08940886.2018.1483653.
[17] V.N. Strocov, L.L. Lev, F. Alarab, P. Constantinou, X. Wang, T. Schmitt, T.J. Z. Stock, L. Nicolaï, J. Očenášek, J. Minár, High-energy photoemission final states beyond the free-electron approximation, Nat. Commun. 14 (2023) 4827, https://doi.org/10.1038/s41467-023-40432-5.
[18] B.P. Tonner, Energy-filtered imaging with electrostatic optics for photoelectron microscopy, Nucl. Instrum. Methods Phys. Res., Sect. A 291 (1990) 60–66.
[19] E. Bauer, C. Koziol, G. Lilienkamp, T. Schmidt, Spectromicroscopy in a low energy electron microscope, J. Electron. Spectrosc. Relat. Phenom. 84 (1997) 201–209, https://doi.org/10.1016/S0368-2048(97)00007-8.
[20] M. Patt, C. Wiemann, N. Weber, M. Escher, A. Gloskovskii, W. Drube, M. Merkel, C. M. Schneider, Bulk sensitive hard x-ray photoemission electron microscopy, Rev. Sci. Instrum. 85 (2014) 113704, https://doi.org/10.1063/1.4902141.
[21] O. Fedchenko, L. Smejkal, M. Kallmayer, Ya. Lytvynenko, K. Medjanik, S. Babenkov, D. Vasilyev, M. Kläui, J. Demsar, G. Schönhense, M. Jourdan, J. Sinova, H.-J. Elmers, Direct observation of antiferromagnetic parity violation in the electronic structure of Mn2Au, J. Phys. Condens. Matter. 34 (2022) 425501, https://doi.org/10.1088/1361648X/ac87e6.
[22] T. Allison, A. Kunin, G. Schönhense, Cavity-enhanced high-order harmonic generation for high-performance time-resolved photoemission experiments, APL Photon. 10 (2025) 010906, https://doi.org/10.1063/5.0244045.
[23] N. Bergeard, M.G. Silly, D. Krizmancic, C. Chauvet, M. Guzzo, J.P. Ricaud, M. Izquierdo, L. Stebel, P. Pittana, R. Sergo, G. Cautero, G. Dufour, F. Rochet, F. Sirotti, Time-resolved photoelectron spectroscopy using synchrotron radiation time structure, J. Synchrotron. Radiat. 18 (2011) 245, https://doi.org/10.1107/S0909049510052301.
[24] M. Hoesch T. K. Kim, P. Dudin, H. Wang, S. Scott, P. Harris, S. Patel, M. Matthews, D. Hawkins, S.G. Alcock, T. Richter, J.J. Mudd, M. Basham, L. Pratt, P. Leicester, E. C. Longhi, A. Tamai, F. Baumberger, A facility for the analysis of the electronic structures of solids and their surfaces by synchrotron radiation photoelectron spectroscopy, Rev. Sci. Instrum. 88 (2017) 013106, https://doi.org/10.1063/1.4973562.
[25] S.V. Borisenko, One-cubed ARPES user facility at BESSY II, Synchrotron. Radiat. News 25 (2012) 6.
[26] G. Kaindl, K. Schulz, P.A. Heimann, J.D. Bozek, A.S. Schlachter, Ultra-high resolution in the soft X-ray region at beamline 9.0.1 at the ALS, Synchrotron. Rad. News 8 (1995) 29, https://doi.org/10.1080/08940889508602839.
[27] J. Miyawaki, K. Fujii, T. Imazono, K. Horiba, Y. Ohtsubo, N. Inami, T. Nakatani, K. Inaba, A. Agui, H. Kimura, Design of ultrahigh energy resolution RIXS beamline at NanoTerasu, J. Phys.: Conf. Ser. 2380 (2022) 012030, https://doi.org/10.1088/1742-6596/2380/1/012030.
[28] C.M. Polley, M. Leandersson, J. Adell, J. Osiecki, D. Carbone, K. Ali, H. Fedderwitz, T. Belasubramanian, The bloch beamline at MAX IV: micro-spot ARPES from a conventional, full-featured beamline, Synchrotron. Rad. News 37 (2024) 1, https://doi.org/10.1080/08940886.2024.2391252.
[29] T. Shimojima, K. Okazaki, S. Shin, Low-temperature and high-energy-resolution laser photoemission spectroscopy, J. Phys. Soc. Japan 84 (2015) 072001, https://doi.org/10.7566/JPSJ.84.072001.
[30] https://www.surface-concept.com/detectors.
[31] A.S. Tremsin, J.V. Vallerga, O.H.W. Siegmund, Overview of spatial and timing resolution of event counting detectors with Microchannel Plates, Nuclear Inst. Methods Phys. Res. A 949 (2020) 162768, https://doi.org/10.1016/j.nima.2019.162768.
[32] A. Vredenborg, W.G. Roeterdink, M.H.M. Janssen, A photoelectron-photoion coincidence imaging apparatus for fs time-resolved molecular dynamics with electron ToF resolution, Rev. Sci. Instrum. 79 (2008) 063108, https://doi.org/10.1063/1.2949142.
[33] W.S. Jung, C.S. Leem, C. Kim, S.R. Park, S.Y. Park, B.J. Kim, E. Rotenberg, C. Kim, Imaging the electron density in solids by using multi-brillouin-zone angle resolved photoelectron spectroscopy, Phys. Rev. B 82 (2010) 235105, https://doi.org/10.1103/PhysRevB.82.235105.
[34] E. McCann, M. Koshino, The electronic properties of bilayer graphene, Rep. Prog. Phys. 76 (2013) 056503, https://doi.org/10.1088/0034-4885/76/5/056503.
[35] S. Moser, A toy model for dichroism in angle resolved photoemission, J. Electron Spectrosc. Relat. Phenom. 262 (2023) 147278, https://doi.org/10.1016/j.elspec.2022.147278.
[36] M. Schüler, T. Pincelli, S. Dong, T.P. Devereaux, M. Wolf, L. Rettig, R. Ernstorfer, S. Beaulieu, Polarization-modulated angle-resolved photoemission spectroscopy: toward circular dichroism without circular photons and bloch wave-function reconstruction, Phys. Rev. X 12 (2022) 011019, https://doi.org/10.1103/PhysRevX.12.011019.
[37] M. Bauernfeind, J. Erhardt, P. Eck, P.K. Thakur, J. Gabel, T.-L. Lee, J. Schäfer, S. Moser, D. Di Sante, R. Claessen, G. Sangiovanni, Design and realization of topological Dirac fermions on a triangular lattice, Nat. Commun. 12 (2021) 5396, https://doi.org/10.1038/s41467-021-25627-y.
[38] C. Schmitt, J. Erhardt, P. Eck, M. Schmitt, K. Lee, P. Keßler, T. Wagner, M. Spring, B. Liu, S. Enzner, M. Kamp, V. Jovic, C. Jozwiak, A. Bostwick, E. Rotenberg, T. Kim, C. Cacho, T.-L. Lee, G. Sangiovanni, S. Moser, R. Claessen, Achieving environmental stability in an atomically thin quantum spin Hall insulator via graphene intercalation, Nat.Commun 15 (2024) 1486, https://doi.org/10.1038/s41467-024-45816-9.
[39] J. Erhardt, C. Schmitt, P. Eck, M. Schmitt, P. Kessler, K. Lee, T. Kim, C. Cacho, I. Cojocariu, D. Baranowski, V. Feyer, L. Veyrat, G. Sangiovanni, R. Claessen, S. Moser, Bias-free access to orbital angular momentum in two-dimensional quantum materials, Phys. Rev. Lett. 132 (2024) 196401, https://doi.org/10.1103/PhysRevLett.132.196401.
[40] S. Tanuma, C.J. Powell, D.R. Penn, Calculations of electron inelastic mean free paths. IX. Data for 41 elemental solids over the 50 eV to 30 keV range, Surf. Interface Anal. 43 (2011) 689, https://doi.org/10.1002/sia.3522.
[41] D. Shoenberg, The fermi surfaces of copper, silver and gold I. The de Haas - van Alphen effect, Phil. Trans. Roy. Soc. A 255 (1962) 85–133. https://www.jstor.org/stable/73177.
[42] D. Shoenberg, Magnetic Oscillations in Metals, Cambridge Univ. Press, 1984, https://doi.org/10.1017/CBO9780511897870.
[43] M.S. Suzuki, I.S. Suzuki, D. Shoenberg, Open Orbits in Copper Fermi Surface, 2017. https://www.researchgate.net/publication/322027719.

[44] O. Fedchenko, K. Medjanik, S. Chernov, D. Kutnyakhov, M. Ellguth, A. Oelsner, B. Schönhense, T. Peixoto, P. Lutz, C.-H. Min, F. Reinert, S. Däster, Y. Acremann, J. Viefhaus, W. Wurth, J. Braun, J. Minár, H. Ebert, H.J. Elmers, G. Schönhense, 4D texture of circular dichroism in soft-x-ray photoemission from tungsten, New J. Phys. 21 (2019) 013017, 1367-2630/aaf4cd.

[45] H. Ryu, I. Song, B. Kim, S. Cho, S. Soltani, T. Kim, M. Hoesch, C.H. Kim, C. Kim, Photon energy dependent circular dichroism in angle-resolved photoemission from Au(111) surface states, Phys. Rev. B 95 (2017) 115144, https://doi.org/10.1103/PhysRevB.95.115144.

[46] O. Fedchenko, A. Winkelmann, K. Medjanik, S. Babenkov, D. Vasilyev, S. Chernov, C. Schlueter, A. Gloskovskii, Yu. Matveyev, W. Drube, B. Schönhense, H.J. Elmers, G. Schönhense, High-resolution hard-X-ray photoelectron diffraction in a momentum microscope - the model case of graphite, New J. Phys. 21 (2019) 113031, https://doi.org/10.1088/1367-2630/ab51fe.

[47] C.S. Fadley, S. Nemsak, Some future perspectives in soft- and hard- X-ray photoemission, J. Electron Spectrosc. Relat. Phenom. 195 (2014) 409, https://doi.org/10.1016/j.elspec.2014.06.004.

[48] S. Kikuchi, The diffraction of cathode rays by mica, in: Proc. Imp. Acad. 4, 354 and 471, 1928, https://doi.org/10.2183/pjab1912.4.271.

[49] A. Winkelmann, C.S. Fadley, F.J. Garcia de Abajo, High-energy photoelectron diffraction: model calculations and future possibilities, New J. Phys. 10 (2008) 113002, https://doi.org/10.1088/1367-2630.

[50] Z.L. Wang, Thermal diffuse scattering in sub-angstrom quantitative electron microscopy—phenomenon, effects and approaches, Micron 34 (2003) 141, https://doi.org/10.1016/s0968-4328(03)00024-6.

[51] A. Winkelmann, B. Schröter, W. Richter, Simulation of high energy photoelectron diffraction using many-beam dynamical Kikuchi-band theory, Phys. Rev. B 69 (2004) 245417, https://doi.org/10.1103/PhysRevB.69.245417.

[52] O. Fedchenko, A. Winkelmann, G. Schönhense, Structure analysis using time-of-flight momentum microscopy with hard X-rays: status and prospects, (invited review), J. Phys. Soc. Jpn. 91 (2022) 091006, https://doi.org/10.7566/JPSJ.91.091006 special volume “Hyper-Ordered Structures”.

[53] O. Tkach, T.P. Vo, O. Fedchenko, K. Medjanik, Y. Lytvynenko, S. Babenkov, D. Vasilyev, Q.L. Nguyen, T. Peixoto, A. Gloskowski, C. Schlueter, M. Hoesch, D. Kutnyakhov, M. Scholz, L. Wenthaus, N. Wind, S. Marotzke, A. Winkelmann, K. Rossnagel, J. Minar, H.-J. Elmers, G. Schönhense, Circular dichroism in hard-X-ray photoelectron kikuchi diffraction observed by ToF momentum microscopy, Ultramicroscopy 250 (2023) 113750, https://doi.org/10.1016/j.ultramic.2023.113750.

[54] G. Schönhense, Circular dichroism and spin polarization in photoemission from adsorbates and non-magnetic solids, Physica Scripta 31 (1990) 255–275, https://doi.org/10.1088/0031-8949/1990/T31/035. T.

[55] T.-P. Vo, O. Tkach, S. Tricot, D. Sébilleau, A. Winkelmann, O. Fedchenko, Y. Lytvynenko, D. Vasilyev, H.-J. Elmers, G. Schönhense, J. Minár, Analyzing core level photoelectrons by diffraction and circular dichroism by means of first-principle scattering calculations, AIP Conf. Proc. 3251 (2024) 020005, https://doi.org/10.1063/5.0234142.

[56] T.-P. Vo, O. Tkach, S. Tricot, D. Sébilleau, J. Braun, A. Pulkkinen, A. Winkelmann, O. Fedchenko, Y. Lytvynenko, D. Vasilyev, H.-J. Elmers, G. Schönhense and J. Minár, Layered multiple scattering approach to hard X-ray photoelectron diffraction: theory and applications, npj Computational Materials, in print (2025); e-print on arXiv:2411.09669 (2024).

[57] D.P. Woodruff, Photoelectron diffraction: past, present and future, J. Electron Spectrosc. Relat. Phenom. 126 (2002) 55, https://doi.org/10.1016/S0368-2048(02)00205-0.

[58] ed. J. Osterwalder, Photoelectron spectroscopy and diffraction, in: K. Wandelt (Ed.), ‘*Handbook on Surface and Interface Science*’, ‘*Handbook on Surface and Interface Science*’, 1, Wiley-VCH, Weinheim, 2011, pp. 151–214, https://doi.org/10.1002/9783527680535.ch5. ed.

[59] T. Matsushita, T. Muro, F. Matsui, N. Happo, S. Hosokawa, K. Ohoyama, A. Sato-Tomita, Y.C. Sasaki, K. Hayashi, Principle and reconstruction algorithm for atomic-resolution holography, J. Phys. Soc. Jpn. 87 (2018) 061002, https://doi.org/10.7566/JPSJ.87.061002.

[60] T. Matsushita, T. Muro, T. Yokoya, K. Terashima, Y. Kato, H. Matsui, N. Maejima, Y. Hashimoto, F. Matsui, Theory for high-angular-resolution photoelectron holograms considering the inelastic mean free path and the formation mechanism of Quasi-Kikuchi band, Phys. Status Solidi B 257 (2020) 2000117, https://doi.org/10.1002/pssb.202000117.

[61] D. Curcio, K. Volckaert, D. Kutnyakhov, S.Y. Agustsson, K. Bühlmann, F. Pressacco, M. Heber, S. Dziarzhytski, Y. Acremann, J. Demsar, W. Wurth, C.E. Sanders, P. Hofmann, Tracking the surface atomic motion in a coherent phonon oscillation, Phys. Rev. B 106 (2022) L201409, https://doi.org/10.1103/PhysRevB.106.L201409.

[62] K. Baumgärtner, M. Reuner, C. Metzger, D. Kutnyakhov, M. Heber, F. Pressacco, C. H. Min, T.R.F. Peixoto, M. Reiser, C. Kim, W. Lu, R. Shayduk, W.M. Izquierdo, G. Brenner, F. Roth, A. Schöll, S. Molodtsov, W. Wurth, F. Reinert, A. Madsen, D. Popova-Gorelova, M. Scholz, Ultrafast orbital tomography of a pentacene film using time-resolved momentum microscopy at a FEL, Nat. Commun. 13 (2022) 2741, https://doi.org/10.1038/s41467-022-30404-6.

[63] J. Maklar, S. Dong, S. Beaulieu, T. Pincelli, M. Dendzik, Y.W. Windsor, R.P. Xian, M. Wolf, R. Ernstorfer, L. Rettig, A quantitative comparison of time-of-flight momentum microscopes and hemispherical analyzers for time and angle-resolved photoemission spectroscopy experiments, Rev. Sci. Instrum. 91 (2020) 123112, https://doi.org/10.1063/5.0024493.

[64] O. Tkach, G. Schönhense, Multi-mode front lens for momentum microscopy: theory, Ultramicr. (2025), https://doi.org/10.1016/j.ultramic.2025.114167. This volume.

[65] O. Tkach, S. Fragkos, Q. Nguyen, S. Chernov, M. Scholz, N. Wind, S. Babenkov, O. Fedchenko, Y. Lytvynenko, D. Zimmer, A. Hloskovskii, D. Kutnyakhov, F. Pressacco, J. Dilling, L. Bruckmeier, M. Heber, F. Scholz, J. A. Sobota, J. D. Koralek, N. Sirica, M. Hoesch, C. Schlueter, L.V. Odnodvorets, Y. Mairesse, K. Rossnagel, H.-J. Elmers, S. Beaulieu and G. Schönhense, Multi-mode front lens for momentum microscopy: experiments, in preparation, e-print on arXiv 2401.10084 (2024).

[66] H.J. Elmers, O. Tkach, Y. Lytvynenko, P. Yogi, M. Schmitt, D. Biswas, J. Liu, S. V. Chernov, M. Hoesch, D. Kutnyakhov, N. Wind, L. Wenthaus, M. Scholz, K. Rossnagel, A. Gloskovskii, C. Schlueter, A. Winkelmann, A. Haghighirad, T.-L. Lee, M. Sing, R. Claessen, M. Le Tacon, J. Demsar, G. Schönhense, O. Fedchenko, Chirality in the Kagome metal CsV3Sb5, Phys. Rev. Lett. 134 (2025) 096401, https://doi.org/10.1103/PhysRevLett.134.096401.

[67] G.K. Jarvis, Y. Song, C.Y. Ng, High resolution pulsed field ionization photoelectron spectroscopy using multibunch synchrotron radiation: time-of-flight selection scheme, Rev. Sci. Instrum. 70 (1999) 2615, https://doi.org/10.1063/1.1149818.